

# Development of a Hybrid Tracer for SPECT and Optical Imaging of Bacterial Infections

Mick M. Welling,<sup>†,‡</sup> Anton Bunschoten,<sup>†,‡</sup> Joeri Kuil,<sup>†</sup> Rob G. H. H. Nelissen,<sup>‡</sup> Freek J. Beekman,<sup>§,||</sup> Tessa Buckle,<sup>†</sup> and Fijis W. B. van Leeuwen<sup>\*,†</sup>

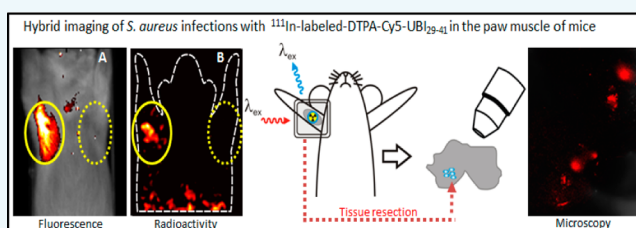
<sup>†</sup>Interventional Molecular Imaging Laboratory, Department of Radiology, and <sup>‡</sup>Department of Orthopedics, Leiden University Medical Center, 2333 ZA Leiden, The Netherlands

<sup>§</sup>Delft University of Technology, 2628 CD Delft, The Netherlands

<sup>||</sup>MILabs, 3584 CX Utrecht, The Netherlands

## S Supporting Information

**ABSTRACT:** In trauma and orthopedic surgery, infection of implants has a major impact on the outcome for patients. Infections may develop either during the initial implantation or during the lifetime of an implant. Both infections, as well as aseptic loosening of the implant, are reasons for revision of the implants. Therefore, discrimination between aseptic-mechanical-loosening and septic-bacterial-loosening of implants is critical during selection of a patient-tailored treatment policy. Specific detection and visualization of infections is a challenge because it is difficult to discriminate infections from inflammation. An imaging tracer that facilitates bacterial identification in a pre- and intraoperative setting may aid the workup for patients suspicious of bacterial infections. In this study we evaluated an antimicrobial peptide conjugated to a hybrid label, which contains both a radioisotope and a fluorescent dye. After synthesis of DTPA-Cy5-UBI<sub>29–41</sub> and—when necessary—radiolabeling with <sup>111</sup>In (yield 96.3 ± 2.7%), in vitro binding to various bacterial strains was evaluated using radioactivity counting and confocal fluorescence microscopy. Intramuscular bacterial infections (*S. aureus* or *K. pneumoniae*) were also visualized in vivo using a combined nuclear and fluorescence imaging system. The indium-111 was chosen as label as it has a well-defined coordination chemistry, and in pilot studies labeling DTPA-Cy5-UBI<sub>29–41</sub> with technetium-99m, we encountered damage to the Cy5 dye after the reduction with SnCl<sub>2</sub>. As a reference, we used the validated tracer <sup>99m</sup>Tc-UBI<sub>29–41</sub>. Fast renal excretion of <sup>111</sup>In-DTPA-Cy5-UBI<sub>29–41</sub> was observed. Target to nontarget (T/NT) ratios were highest at 2 h post injection: radioactivity counting yielded T/NT ratios of 2.82 ± 0.32 for *S. aureus* and 2.37 ± 0.05 for *K. pneumoniae*. Comparable T/NT ratios with fluorescence imaging of 2.38 ± 0.09 for *S. aureus* and 3.55 ± 0.31 for *K. pneumoniae* were calculated. Ex vivo confocal microscopy of excised infected tissues showed specific binding of the tracer to bacteria. Using a combination of nuclear and fluorescence imaging techniques, the hybrid antimicrobial peptide conjugate DTPA-Cy5-UBI<sub>29–41</sub> was shown to specifically accumulate in bacterial infections. This hybrid tracer may facilitate integration of noninvasive identification of infections and their extent as well as real-time fluorescence guidance during surgical resection of infected areas.



## INTRODUCTION

Loosening may develop during the lifetime of orthopedic implants (i.e., artificial joints) and can be associated with incapacitating pain for the patient. The main reasons for these complications are infection of the implant and aseptic loosening as a result of wear debris periprosthetic reaction, both resulting in implant failure.<sup>1</sup> Although it is difficult to differentiate between the two types, the origin of the implant failure is vital during selection of the treatment.<sup>2–4</sup> An imaging technique that facilitates both specific detection and localization of bacteria may help refine the treatment for implant failure.

In routine clinical practice, the presence of invasive pathogens is determined by indirect measures like radiologic imaging and hematologic analysis, as well as by culturing of blood samples in the case of sepsis and by culturing joint effusion samples and tissue biopsies taken during surgery.

Unfortunately, these techniques can yield false negative results, which is even true for growth of microorganisms from tissue biopsies in culture media. One of the problems is that when taking percutaneous biopsies it is often hard to localize the pathogens. Although DNA sequencing technologies can be used to improve the sensitivity of detection, we believe imaging is the best tool to noninvasively localize and diagnose bacterial infections. Noninvasive clinical imaging by radiographs, CT, echography, and/or MRI can only be used to detect late morphological changes that are a result of the infection. As a consequence, there is a need for techniques that can sensitively detect infections in a noninvasive manner. Tracers such as

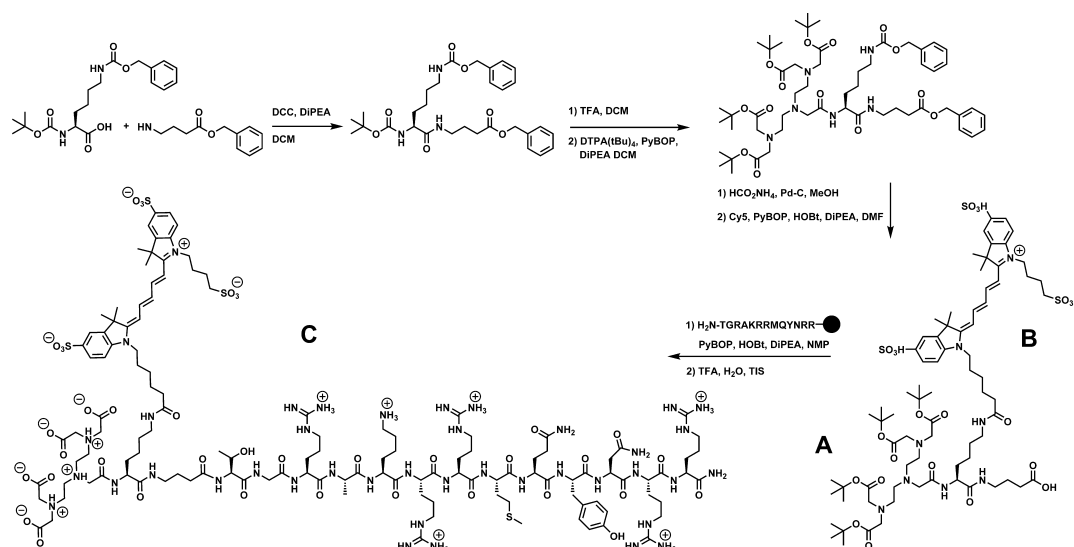
Received: January 29, 2015

Revised: April 7, 2015

Published: April 8, 2015



**Scheme 1. Schematic Presentation of Solid-Phase Peptide Synthesis (SPPS) of Hybrid UBI<sub>29-41</sub> and Structure of the (A) Fluorescent Cy5 Dye, (B) DTPA Chelator, and (C) UBI<sub>29-41</sub> Antimicrobial Peptide<sup>a</sup>**



<sup>a</sup>Covalent conjugation of the hybrid label to the UBI<sub>29-41</sub> peptide (+7 at neutral pH) alters the net charge of the peptide. DTPA-Cy5-UBI<sub>29-41</sub> has a net charge at neutral pH of +3.

<sup>67</sup>Ga-citrate, radiolabeled leukocytes, or <sup>18</sup>F-FDG can accumulate in sites of infection with higher sensitivity; unfortunately, the specificity of these technologies is limited. Discrimination between infections and sterile inflammation is especially a challenge.<sup>5,6</sup>

Only a limited number of bacteria-specific tracers for molecular imaging modalities such as SPECT, PET, and fluorescence imaging have been reported.<sup>7,8</sup> One of these pathogen-specific tracers is based on the synthetic antimicrobial peptide UBI<sub>29-41</sub>. This (positively charged) peptide targets the (negatively charged) membranes of both Gram-positive and Gram-negative bacteria and through this mechanism accumulates in infected tissues in both animals and humans.<sup>9,10</sup> This property makes it a solid platform for further chemical modification. Positive results were obtained for <sup>99m</sup>Tc-UBI<sub>29-41</sub> (SPECT tracer),<sup>11</sup> <sup>68</sup>Ga-NOTA-UBI<sub>29-41</sub> (PET-tracer),<sup>12</sup> and UBI<sub>29-41</sub> labeled with a near-infrared fluorescent dye.<sup>13</sup>

The combination of preoperative noninvasive nuclear imaging and intraoperative surgical fluorescence guidance based on a single imaging agent was shown to be of value in the field of surgical oncology (sentinel node procedures).<sup>14–16</sup> Although their use, as of yet, remains confined to the preclinical setting, a variety of peptide based hybrid imaging tracers have also been described and our group has been involved in the design and successful evaluation of compounds for, e.g., the CXCR4-receptor and  $\alpha_v\beta_3$ -integrin.<sup>17–19</sup> Given the clinical requirements in the field of infection imaging, it seems logical to apply this hybrid-labeling technology to the UBI<sub>29-41</sub> peptide. The nuclear radioisotope on the molecule can then be used to noninvasively establish the onset of a bacterial infection, while the fluorescent component on the molecule allows detection of the bacteria during the intervention and even in the resected (tissue) specimen. In clinical studies, this “hybrid” approach was shown to be highly effective in the imaging and surgical removal of lymph nodes in drainage studies using <sup>99m</sup>Tc-ICG-nanocolloid.<sup>20</sup>

In this manuscript we describe the design, synthesis, and in vitro and in vivo evaluation of the hybrid imaging agent <sup>111</sup>In-DTPA-Cy5-UBI<sub>29-41</sub> for specific identification of bacterial infections.

## RESULTS

**Synthesis and Labeling of the Hybrid Tracer.** A new type of hybrid label, consisting of a DTPA capable of chelating the radioisotope <sup>111</sup>In, and a Cy5 fluorescent dye ( $\lambda_{\text{ex}} = 650$  nm,  $\lambda_{\text{em}} = 670$  nm), was successfully synthesized (Scheme 1). The indium-111 moiety chosen for DTPA conjugation and labeling has a well-defined chemistry, and in pilot studies, we encountered damage to the Cy5 dye after labeling DTPA-Cy5-UBI<sub>29-41</sub> with technetium-99m reduced by SnCl<sub>2</sub>. Also, indium-111 labeled compounds have shown efficacy in nuclear imaging, e.g., tumor imaging with Octeotide and inflammation with indium-111 labeled white blood cells.<sup>21</sup>

Different from the hybrid label that was described previously by Shao et al. and Kuil et al. (2011), this particular label was synthesized in solution and makes use of an asymmetric rather than a symmetric Cy5 dye.<sup>22,18</sup> On top we introduced sulfonate groups on the indole moieties of the dye in an attempt to minimize interaction between the dye and native proteins.<sup>19</sup> The UBI<sub>29-41</sub> peptide (TGRAKRRMQYNRR) was synthesized using standard Fmoc solid phase peptide synthesis (SPPS), and in a last step, the hybrid label was conjugated to the N-terminus of the UBI<sub>29-41</sub> peptide residing on the solid support via the C-terminus of the hybrid scaffold. The identity of the final product DTPA-Cy5-UBI<sub>29-41</sub> was confirmed by mass spectrometry and its purity was more than 95%, as determined by HPLC (Supporting Information Figures S1 and S2). The covalent conjugation of the chelating moiety (overall charge of −1 at pH 6–7 both with and without chelated indium ions)<sup>23</sup> and dye (charge −2) to the UBI<sub>29-41</sub> peptide (+7 at neutral pH) changes the net charge of the peptide to +3. Radiolabeling of the hybrid tracer with <sup>111</sup>In yielded <sup>111</sup>In-DTPA-Cy5-UBI<sub>29-41</sub> (96.3 ± 2.7% labeling efficiency). Also, we assessed the stability of <sup>111</sup>In-DTPA-Cy5-UBI<sub>29-41</sub> which showed no

significant release of the radiolabel until 24 h after labeling. After challenging  $^{111}\text{In}$ -DTPA-Cy5-UBI<sub>29–41</sub> in 50% fetal calf serum for 24 h at 37 °C, we observed <5% release of the radioisotope.

**In Vitro Analysis.** The binding capacity of DTPA-Cy5-UBI<sub>29–41</sub> to Gram-positive (*S. aureus*, *S. epidermidis*, and *B. subtilis*) and Gram-negative (*K. pneumoniae* and *E. coli*) bacteria was evaluated in vitro. Confocal microscopy revealed highly similar tracer uptake in the five strains tested (Figure 1).

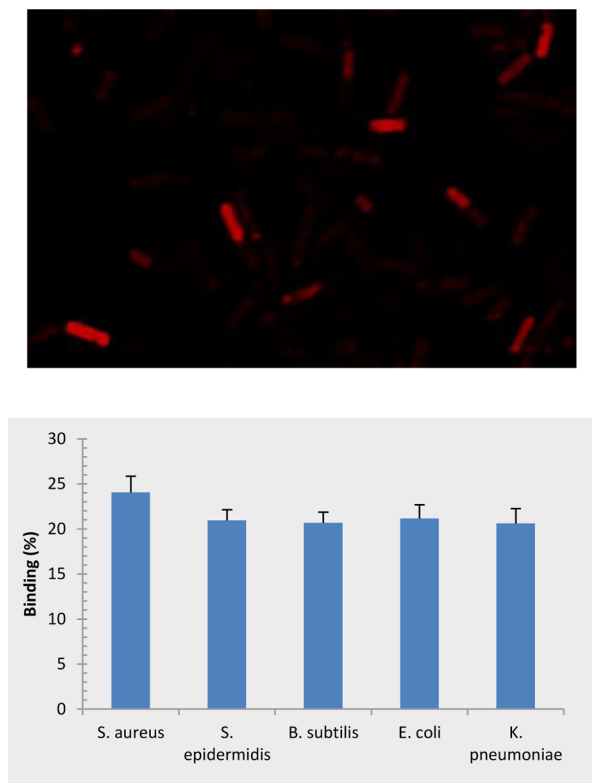


**Figure 1.** Confocal microscopy images (at 1000× magnification) confirming binding of  $^{111}\text{In}$ -DTPA-Cy5-UBI<sub>29–41</sub> to (top panel) *E. coli*. (bottom panel) Quantitative binding of  $^{111}\text{In}$ -DTPA-Cy5-UBI<sub>29–41</sub> to various Gram-positive and Gram-negative bacteria strains.

Binding of DTPA-Cy5-UBI<sub>29–41</sub> appears to be associated with the outer membrane, confirming the proposed binding mechanism. The resolution obtained with the confocal microscope (at 1000× magnification) is not high enough to fully exclude internalization of the peptide. In addition to the fluorescence experiment, binding of  $^{111}\text{In}$ -DTPA-Cy5-UBI<sub>29–41</sub> to  $2 \times 10^8$  colony forming units (CFU) of the five bacterial strains was quantified by a gamma counting procedure that has been described previously for  $^{99\text{m}}\text{Tc}$ -UBI<sub>29–41</sub>.<sup>9</sup> This experiment confirmed binding of the hybrid tracer to the different bacterial strains (Figure 1).

**MTT Toxicity Assay.** After incubating GEB3 cells with either DTPA-Cy5-UBI<sub>29–41</sub> or UBI<sub>29–41</sub>, using concentrations ranging between 0 and 118  $\mu\text{M}$  ( $N = 4$  for each concentration), no significant changes in the cell growth and the normalized MTT absorbance values were observed (Supporting Information Figure S3), indicating these amounts of UBI<sub>29–41</sub> peptides did not evoke toxic side effects on the growth and functionality of these cells.

**Imaging Experiments.** The most important feature of the hybrid approach that uses  $^{111}\text{In}$  and Cy5 as imaging labels is that it allows both SPECT and fluorescence imaging in vivo.<sup>24</sup> Gram-positive *S. aureus* or Gram-negative *K. pneumoniae* were injected in a muscle of mice, and 18 h after inoculation of the bacteria, the mice were injected intravenously with  $^{111}\text{In}$ -DTPA-Cy5-UBI<sub>29–41</sub>. First, the ability to noninvasively identify infections was assessed by recording a total body SPECT/CT image. Infections with both *S. aureus* and *K. pneumoniae* were visible at 2 h post injection (Figure 2). Between the two bacterial strains no remarkable differences in tracer uptake could be observed. After SPECT imaging, the mice were imaged with the fluorescence modality of the U-SPECT-BioFluo and the imaging system was capable of detecting the fluorescent signal originating from the infected muscles with the fur still in place (Figure 2).<sup>25</sup> After U-SPECT-BioFluo imaging, the mice were imaged with the IVIS Spectrum. Since the fur caused additional attenuation of the fluorescent emission, it was removed from the muscles to allow for more detailed fluorescence imaging (Supporting Information Figure S4).

**In Vivo Experiments.** After in vivo imaging, the mice were sacrificed and the organs were dissected to quantify both the radioactive and optical signals originating from various organs

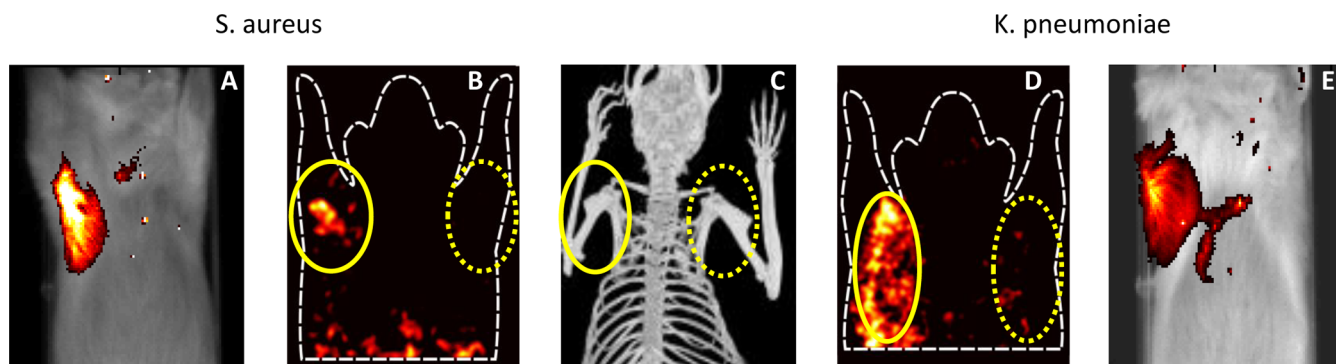


**Figure 2.** Typical in vivo imaging of *S. aureus* or *K. pneumoniae* infections with  $^{111}\text{In}$ -DTPA-Cy5-UBI<sub>29–41</sub> in the paw muscle in mice; images are obtained from volume rendered reconstructions of 0.2 mm slices of a selected region of paws and thigh muscles infected with  $(1–2) \times 10^7$  CFU of bacteria at 2 h after injection of the tracer. On the anterior images, infected muscles are indicated with oval shapes and the contralateral noninfected muscles are indicated with dotted oval shapes (B,D). We included a CT scan of a mouse (C) to clarify the anatomical localization of the infected tissues. Fluorescent imaging of  $^{111}\text{In}$ -DTPA-Cy5-UBI<sub>29–41</sub> in mice with a bacterial (A,E) infection in the right paw at 2 h after injection. Imaging was performed with an integrated radionuclide, bioluminescence, and fluorescence platform (U-SPECT-BioFluo, MILabs).

Table 1. Biodistribution of Radiolabeled UBI<sub>29–41</sub> in Mice with Bacterially Infected Muscles<sup>a</sup>

tissue	<sup>111</sup> In-DTPA-Cy5-UBI <sub>29–41</sub>		<sup>99m</sup> Tc-UBI <sub>29–41</sub>	
	<i>S. aureus</i>	<i>K. pneumoniae</i>	<i>S. aureus</i>	<i>K. pneumoniae</i>
noninfected muscle	1.6 ± 0.6	1.3 ± 0.4	1.0 ± 0.2	0.6 ± 0.1
infected muscle	2.8 ± 0.9	2.8 ± 0.8	2.0 ± 0.2	1.0 ± 0.4
heart	2.4 ± 1.2	1.8 ± 0.8	2.3 ± 0.4	1.4 ± 0.4
lungs	3.1 ± 1.7	3.7 ± 2.3	2.4 ± 0.4	1.1 ± 0.4
liver	1.4 ± 0.7	1.6 ± 0.8	1.2 ± 0.7	0.7 ± 0.2
spleen	2.8 ± 1.1	2.9 ± 1.1	4.6 ± 1.3	3.6 ± 1.3
kidneys	25.8 ± 4.1	20.1 ± 3.5	9.1 ± 7.8*	9.6 ± 1.9*
stomach	0.9 ± 0.7	0.8 ± 0.4	0.3 ± 0.1	0.2 ± 0.02
intestines	0.9 ± 0.5	0.9 ± 0.5	0.6 ± 0.3	0.3 ± 0.1
brain	0.04 ± 0.02	0.04 ± 0.01	0.08 ± 0.02	0.06 ± 0.01
activity excreted in urine (%ID)	69.3 ± 2.0			
activity excreted in feces (%ID)	<0.01		<0.01	

<sup>a</sup>Data (expressed as the mean ± SEM of the percentage of the injected dose per gram tissue of at least 5 observations) are calculated from radioactivity counts in various tissues (%ID/g) of various tissues at 2 h post-injection of the tracer. For both tracers, no significant differences were found between the tissue uptake values in mice infected with either *S. aureus* or *K. pneumoniae*. \* = *p* < 0.05 (*t*-test) compared to <sup>111</sup>In-DTPA-Cy5-UBI<sub>29–41</sub>.

and tissues. Table 1 shows the biodistribution based on gamma counting (%ID/g tissue) of <sup>111</sup>In-DTPA-Cy5-UBI<sub>29–41</sub> and <sup>99m</sup>Tc-UBI<sub>29–41</sub> in bacterially infected mice at 2 h after administration of the tracers. No significant differences were found between mice infected with either *S. aureus* or *K. pneumoniae*. Both tracers were cleared via the renal pathway with blood half-lives of 13.4 ± 5.9 min for <sup>111</sup>In-DTPA-Cy5-UBI<sub>29–41</sub> and 16.4 ± 2.3 min for <sup>99m</sup>Tc-UBI<sub>29–41</sub>; at 2 h after injection 69.3 ± 2.1% of the injected dose was excreted with the urine for <sup>111</sup>In-DTPA-Cy5-UBI<sub>29–41</sub> and 86.4 ± 8.4% for <sup>99m</sup>Tc-UBI<sub>29–41</sub> which was significantly higher (*P* < 0.05). However, for <sup>111</sup>In-DTPA-Cy5-UBI<sub>29–41</sub> we observed a significantly higher (*P* < 0.05) retention in the kidneys compared to <sup>99m</sup>Tc-UBI<sub>29–41</sub> (Table 1). The biodistribution results of <sup>111</sup>In-DTPA-Cy5-UBI<sub>29–41</sub> otherwise showed a similar pattern to that of <sup>99m</sup>Tc-UBI<sub>29–41</sub>. It is noteworthy that, except for the spleen, the background activity of <sup>111</sup>In-DTPA-Cy5-UBI<sub>29–41</sub> in all other tissues was slightly higher at each time point tested, but the differences were not significant. Infected muscle to noninfected muscle (T/NT) ratios calculated from the %ID/g tissue were highest at 2 h post injection, namely, for <sup>111</sup>In-DTPA-Cy5-UBI<sub>29–41</sub> 2.8 ± 0.3 for *S. aureus* and 2.4 ± 0.1 for *K. pneumoniae* (Table 2). Hence, this time interval was considered the most ideal for imaging. Additionally, in our animal experiments we did not observe any adverse effects as a result of the injection of the tracers.

Ex vivo analysis of the fluorescent signal from infected and noninfected muscles also showed the highest T/NT ratios at 2 h post injection, 2.4 ± 0.1 for *S. aureus* and 3.6 ± 0.1 for *K. pneumoniae* (Table 2). Due to scattering and the attenuation limitations of fluorescence imaging, calculating the uptake of the tracer in various tissues as a percentage of the injected dose (%ID) based on a fluorescent signal is not representative for biodistribution and quantification studies.

After macroscopic fluorescence imaging of the various organs (Table 2 and Figure S4), they were further processed for microscopic analysis. Inspection of 1 mm slices revealed fluorescent *S. aureus* and *K. pneumoniae* alongside the muscle fibers (Figure 3). Higher magnification on unstained 60 μm cryo-sections revealed fluorescent clusters within the infected tissue only. For reference, we performed hematoxylin-eosin (HE) and Gram staining on serial sections to depict the *S.*

Table 2. Accumulation of <sup>111</sup>In-DTPA-Cy5-UBI<sub>29–41</sub> or <sup>99m</sup>Tc-UBI<sub>29–41</sub> in Bacterially Infected Muscles in Mice<sup>a</sup>

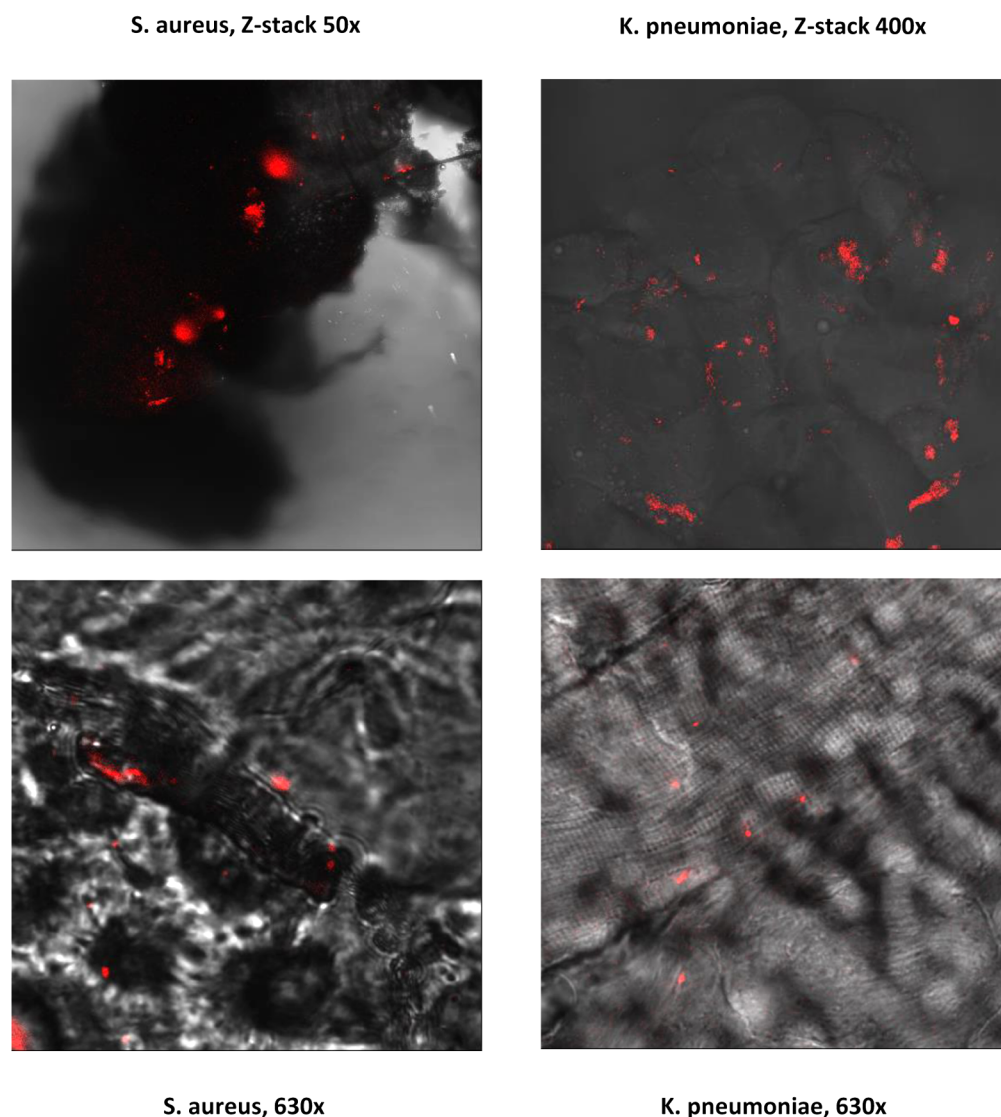
time p.i.	counting	T/NT ratio	
		<i>S. aureus</i>	<i>K. pneumoniae</i>
1 h	<sup>111</sup> In	1.72 ± 0.10	1.99 ± 0.10
	<sup>99m</sup> Tc	1.78 ± 0.28	1.96 ± 0.23
	fluorescence <sup>#</sup>	1.20 ± 0.13	1.71 ± 0.21
2 h	<sup>111</sup> In	2.82 ± 0.45	2.37 ± 0.19
	<sup>99m</sup> Tc	3.64 ± 0.60	2.91 ± 0.58
	fluorescence <sup>#</sup>	2.38 ± 0.09	3.55 ± 0.31
24 h	<sup>111</sup> In	1.68 ± 0.05	1.44 ± 0.04
	<sup>99m</sup> Tc	ND	ND
	fluorescence <sup>#</sup>	ND	ND

<sup>a</sup>Data are expressed as the mean ± SEM target to non-target ratio (T/NT) calculated from radioactivity counts (%ID/g) or photons (<sup>#</sup> = average radiance photons/s/cm<sup>2</sup>/sr) from entirely excised muscles at various intervals post-injection of the tracer (*n* = 4). ND = not determined. <sup>#</sup> Ratios calculated from regions of interest drawn over the infected muscles after removing of the fur and skin on fluorescence images (Ex = 640 nm, Em = 700 nm for 1 s). For both radioactive tracers, no significant differences were found between the T/NT ratios in mice infected with either *S. aureus* or *K. pneumoniae*.

*aureus* colonies present in infected muscles (Figure 4). Co-localization was observed between white blood cells (HE staining) and the presence of bacteria (Gram staining). In control (noninfected tissue), no fluorescent signals or bacterial clusters were observed (data not shown).

To further confirm the presence (and outgrowth) of the bacterial infections, a part of the excised infected muscles were homogenized and serial dilutions were cultured to determine the number of bacteria in these tissues. Between the two bacterial strains, a nearly 3-fold difference was calculated in bacterial outgrowth per gram tissue of (8.0 ± 4.2) × 10<sup>8</sup> CFU for *S. aureus* and (2.5 ± 1.0) × 10<sup>8</sup> CFU for *K. pneumoniae* (*P* < 0.001), which indicates (with comparable T/NT ratios of the tracer for both strains) a slightly better binding of the tracer to *K. pneumoniae* in mice.





S. aureus, Z-stack 50x

K. pneumoniae, Z-stack 400x

S. aureus, 630x

K. pneumoniae, 630x

**Figure 3.** Confocal microscopic analysis of DTPA-CyS-UBI<sub>29–41</sub> in bacterially infected muscles. Low magnification (50×) was performed on 1-mm-thick sections, whereas high magnification (400× or 630×) was performed on 60-μm-thick cryo sections.

## DISCUSSION

Specific targeting and imaging of infections may aid the surgeon in clinical localization and diagnosis of persisting (orthopedic) infections. The present study investigated the feasibility of the hybrid imaging technology, recently introduced in the field of oncologic imaging,<sup>14,15</sup> for infection imaging. Our main finding for the hybrid bacterial tracer <sup>111</sup>In-DTPA-CyS-UBI<sub>29–41</sub> was the ability to identify a bacterial infection in vivo using both radioactive and fluorescent imaging.

Binding of UBI<sub>29–41</sub> with the negatively charged outer leaflet of bacteria is in part based on electrostatic interactions.<sup>26</sup> The binding of UBI<sub>29–41</sub> to bacteria is, however, significantly reduced for a scrambled version of this peptide, suggesting that the amino acid sequence also plays an important role.<sup>27</sup> Conjugation of the hybrid label to the UBI<sub>29–41</sub> peptide reduces the net charge of the tracer from +7 to +3 (Scheme 1) and introduces polarity in the molecule; one side of the tracer is positively charged, while the side containing the hybrid label is negatively charged. Our data suggests that this evident alteration in the net charge of the tracer has minimal influence on the ability of the peptide part of the tracer to target bacteria.

In fact, it may even help reduce the amount of nonspecific interactions that are associated with positively charged imaging agents (e.g., uptake in apoptotic cells, regenerating bone, and cartilage).<sup>28,29</sup>

Earlier studies noted that alterations of UBI<sub>29–41</sub> can cause differences in the distribution profiles. For example, studies with hydrazinonicotinamide (HYNIC) conjugation to UBI<sub>29–41</sub> showed similar renal clearance as for directly <sup>99m</sup>Tc-labeled UBI<sub>29–41</sub>, while the N<sub>2</sub>S<sub>2</sub>-conjugated <sup>99m</sup>Tc-UBI<sub>29–41</sub> derivative gave hepatobiliary rather than renal excretion.<sup>30</sup> Other studies performed with either <sup>68</sup>Ga-NOTA-UBI<sub>29–41</sub> for PET or ICG-02-UBI<sub>29–41</sub> did not provide biodistribution data as the %ID/g tissue, but from imaging reports clearance of the tracer mainly occurred by the kidneys.<sup>12,13</sup> In our study we found that introduction of the DTPA-CyS moiety increased renal uptake for the UBI<sub>29–41</sub> conjugate. As shown in Table 1 for <sup>111</sup>In-DTPA-CyS-UBI<sub>29–41</sub> the retention of activity in the kidneys was 20.1–25.6%ID/g kidneys, but for <sup>99m</sup>Tc-UBI<sub>29–41</sub> this was lower (9.1–9.6%ID/g). Moreover, compared to <sup>99m</sup>Tc-UBI<sub>29–41</sub>, <sup>111</sup>In-DTPA-CyS-UBI<sub>29–41</sub> showed higher amounts of radioactivity in background tissues, which indicates that the

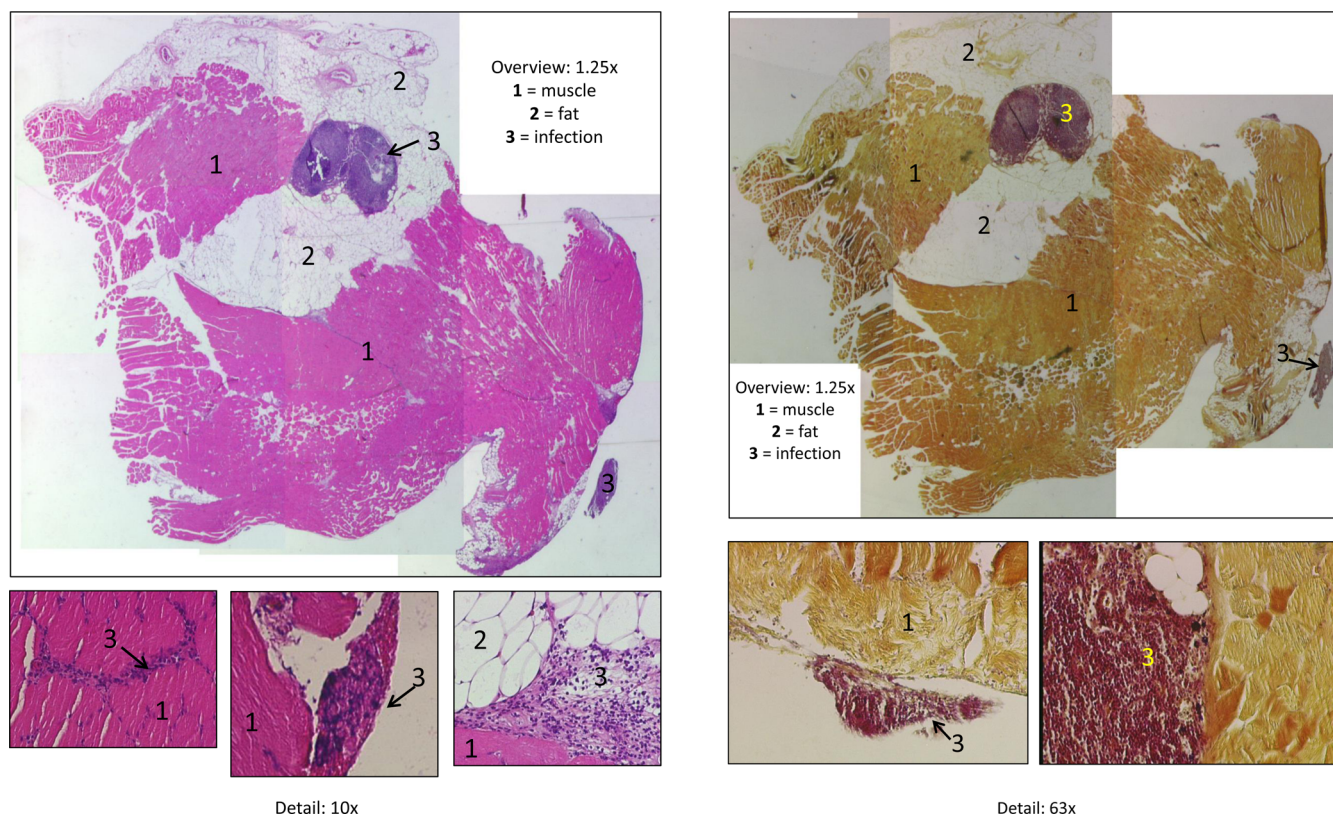


**Figure 4.** Light microscopy of *S. aureus* infected muscles in mice. HE staining on serial 4  $\mu$ m sections of the infected muscles was performed to depict bacterial colonies present in these tissues. Detailed images (63 $\times$  magnification) were taken from the composed overview section.

hybrid UBI peptide was cleared less efficiently from the body. Slower clearance of  $^{111}\text{In}$ -DTPA-Cy5-UBI<sub>29–41</sub> was also emphasized by the reduced amount of radioactivity excreted with urine ( $69.3 \pm 2.0\%$ ID) compared to  $86.4 \pm 4.2\%$ ID for  $^{99\text{m}}\text{Tc}$ -UBI<sub>29–41</sub>. Most likely this is not an effect of size based filtering as the two tracers are comparable in size. We hypothesized that differences in glomerular filtration depend on charge interactions between the tracers and the glomerular basement membrane, but we could not support this with evidence. Likely, cationic compounds such as  $^{99\text{m}}\text{Tc}$ -UBI<sub>29–41</sub> (+7) are more readily filtered than equally sized but less positively charged tracers such as  $^{111}\text{In}$ -DTPA-Cy5-UBI<sub>29–41</sub> (+3). Despite the fast clearance of radiolabeled UBI<sub>29–41</sub> peptides in this and former preclinical infection imaging studies with half-lives of about 15 min, this clearance does not prevent the fast targeting of pathogens.<sup>31,12</sup> Also, in clinical studies  $^{99\text{m}}\text{Tc}$ -UBI<sub>29–41</sub> was rapidly excreted but still showed fast detection of infected tissues as well, which indicates that in vivo interaction of the tracer with pathogens is sufficient to provide an image of the infection.

The influence of the dye is markedly different from the hepatic clearance we previously observed for hybrid agents functionalized with the CyAL-5.5<sub>b</sub> dye, a dye that seems to induce interactions with proteins.<sup>18,19</sup> This said, ideally introduction of an imaging label should not influence the biodistribution of the UBI<sub>29–41</sub> backbone at all. Nevertheless, the data from bacterial binding experiments were in concordance with earlier bacteria targeting studies using  $^{99\text{m}}\text{Tc}$ -UBI<sub>29–41</sub> (Table 2).<sup>9</sup> In vivo the chemical modification of UBI<sub>29–41</sub> and differences in clearance still allowed targeting of bacteria with T/NT ratios (on average T/NT  $\leq 3$ ) that are

highly similar to that of  $^{99\text{m}}\text{Tc}$ -UBI<sub>29–41</sub>. This observation suggests that in our study the placement of the hybrid imaging moiety is positioned on the UBI<sub>29–41</sub> backbone where it does not interfere with the peptide interactions with bacterial surfaces.

Through the availability of a hybrid-UBI<sub>29–41</sub> tracer, we have also been able to compare the advantages and disadvantages of fluorescence imaging. For one, due to scattering and absorption, fluorescence imaging provides a maximum penetration depth of 1 cm in tissue.<sup>32</sup> Hence, whole body fluorescence imaging may provide misleading results.<sup>25</sup> Also, determining the biodistribution as a percentage of the injected dose/gram (%ID/g) cannot be accurately done using fluorescence. For both these features we find the nuclear imaging/detection technologies superior. On the other hand, fluorescence imaging can provide detailed imaging at the microscopic level and during surgery can provide real-time feedback. In this respect, the advantage of a hybrid tracer that combines the positive features of both imaging modalities is evident. Ongoing studies with ICG- $^{99\text{m}}\text{Tc}$ -nanocolloid emphasize that the hybrid approach is superior to the individual approaches.

Regarding the safety of injecting  $^{99\text{m}}\text{Tc}$ -labeled UBI<sub>29–41</sub> peptides in animals, even after repeated injections no side effects were reported for doses up to 40 mg/kg.<sup>33</sup> Additionally, from at least 10 patient studies on the imaging of infection in clinical situations such as osteomyelitis, soft tissue infections, spondylitis, fever of unknown origin, prosthesis, and endocarditis high sensitivities and specificities were reported. No side effects were reported, indicating that in humans UBI<sub>29–41</sub> is also well tolerated.<sup>10,34</sup> However,  $^{111}\text{In}$ -DTPA-Cy5-UBI<sub>29–41</sub> is basically a different molecule. To exclude possible



side effects of this new tracer we compared the dose–response effect of DTPA-Cy5-UBI<sub>29–41</sub> with UBI<sub>29–41</sub> on a human epithelial cell line using the 3-(4,5-dimethylthiazol-2-yl)-2,5-diphenyltetrazolium bromide (MTT) viability assay.<sup>35</sup> From these experiments it became clear that in vitro 0.1 mM of both peptides are well tolerated by this human cell line for 24 h at 37 °C (Supporting Information Figure S3). This dose is much higher than what can be locally achieved after i.v. injection of the compounds into mice due to the immediate dilution in blood and following rapid excretion. Furthermore, during the experiments we observed no adverse effects of injecting the tracers.

UBI<sub>29–41</sub> is capable of binding multiple bacterial strains and is thereby possibly a good broad spectrum imaging agent that can be used to indicate the presence of most bacteria; in many cases finding and removing the infection is the main purpose of the imaging routine. As with many other infection imaging tracers, <sup>111</sup>In-DTPA-Cy5-UBI<sub>29–41</sub> is generic. From earlier studies with UBI<sub>29–41</sub>, we also know that this peptide binds bacteria irrespective of their drug resistance.<sup>9,36</sup> It can, however, not differentiate between pathogens; for that, other tracers will have to be developed, e.g., strain specific or revealing the presence of certain proteases.<sup>7</sup> Regarding the sensitivity of this tracer, the outgrowth of bacteria in patients depends on many factors including the availability of nutrients and hiding from and elimination by the host immune system. Also, the infection is not always limited to a single lesion. From earlier studies with <sup>99m</sup>Tc-UBI<sub>29–41</sub> imaging the effect of antimicrobial therapy allowed visualization of the significant reduction of bacterial numbers from 10<sup>7</sup> viable bacteria to 10<sup>3</sup> viable bacteria,<sup>36</sup> which makes this tracer a very sensitive one; however, this was not assessed for <sup>111</sup>In-DTPA-Cy5-UBI<sub>29–41</sub>.

## CONCLUSIONS

We have synthesized and characterized a hybrid <sup>111</sup>In-DTPA-Cy5-UBI<sub>29–41</sub>. Preclinical evaluation of this tracer emphasizes its ability to visualize individual bacteria by microscopy in excised tissues, as well as bacterial infections. This tracer may facilitate integration of diagnostic nuclear imaging and real-time fluorescence guidance during surgical interventions aimed at removal of the infected tissue, during, e.g., treatment of infected implants or infected native joints and bone. As such, it not only expands the application of the UBI<sub>29–41</sub> peptide, but more importantly it may enable a higher success rate of debridement of infected tissue in the presence of a well fixed orthopedic implant, subsequently with no need to remove the implant, and thus lower morbidity to the patient.

## EXPERIMENTAL PROCEDURES

**General.** All chemicals were obtained from commercial sources and used without further purification. The reactions were monitored by thin layer chromatography (TLC). High pressure liquid chromatography (HPLC) was performed on a Waters HPLC system (Waters Chromatography B.V., Etten-Leur, The Netherlands) using a 1525EF pump and a 2489 UV detector. For preparative HPLC, a Maisch Repro Sil-Pur 120 C18-AQ 10 μM (250 mm × 20 mm) column (Dr. Maisch HPLC GmbH, Ammerbuch-Entringen, Germany) was used at a flow rate of 12 mL/min. For semipreparative HPLC a Maisch Repro Sil-Pur C18-AQ 10 μM (250 mm × 10 mm) column was used (5 mL/min). For analytical HPLC a Maisch Repro Sil-Pur C18-AQ 5 μM (250 mm × 4.6 mm) column was used with a

gradient of 0.1% TFA in H<sub>2</sub>O/CH<sub>3</sub>CN 95:5 to 0.1% TFA in H<sub>2</sub>O/CH<sub>3</sub>CN 5:95 in 20 min (1 mL/min). Mass spectrometry was performed on a Bruker microflex MALDI-TOF mass spectrometer. NMR spectra were taken using a Bruker DPX-300 spectrometer (300 MHz <sup>1</sup>H NMR, 75 MHz <sup>13</sup>C NMR) and the chemical shifts are given in ppm (δ) relative to tetramethylsilane (TMS). Abbreviations used include singlet (s), doublet (d), doublet of doublets (dd), triplet (t), and unresolved multiplet (m).

**Boc-Lys(Cbz)-Abu-OBn.** Boc-Lys(Cbz)-OH (7.61 g, 20 mmol) and benzyl 4-aminobutanoate *p*-tosylate (H-γ-Abu-OBn-*p*-tosylate, 7.31 g, 20 mmol) were dissolved in CH<sub>3</sub>CN (250 mL) and DiPEA (3.40 mL, 20 mmol) was added. The solution was cooled to 0 °C before DCC (4.33 g, 21 mmol) was added. The mixture was stirred over the weekend at room temperature. The suspension was filtered and the filtrate was concentrated. EtOAc was added to the residue and the organic phase was washed with 5% NaHCO<sub>3</sub> solution (3×), 5% citric acid solution (3×), and brine; dried with Na<sub>2</sub>SO<sub>4</sub>; filtered; and concentrated. The product was purified with column chromatography (gradient of EtOAc/hexane 1:1 to EtOAc/hexane 2:1) yielding 5.8 g (10.4 mmol, 52%) of a yellowish oil that slowly became solid. MS: [M + Na]<sup>+</sup> calculated 578.3, found 578.0; [M + K]<sup>+</sup> calculated 594.4, found 594.0. <sup>1</sup>H NMR (CDCl<sub>3</sub>, 300 MHz) δ = 1.35 (m, 2H, CH<sub>2</sub>), 1.42 (s, 9H, tBu), 1.48 (m, 2H, CH<sub>2</sub>), 1.56 (m, 2H, CH<sub>2</sub>), 1.81 (m, 2H, CH<sub>2</sub>), 2.39 (t, 2H, CH<sub>2</sub>), 3.17 (dd, 2H, CH<sub>2</sub>), 3.27 (dd, 2H, CH<sub>2</sub>), 4.00 (m, 1H, CH), 4.97 (m, 1H, NH), 5.08, 5.10 (2 s, 4H, 2 CH<sub>2</sub> benzyl), 5.19 (m, 1H, NH), 6.49 (m, 1H, NH), 7.34 (m, 10H, Ar). <sup>13</sup>C NMR (CDCl<sub>3</sub>, 75 MHz) δ = 22.6, 24.7, 29.6, 31.7, 32.0, 38.9, 40.5 (7 CH<sub>2</sub>), 28.4 (3 CH<sub>3</sub>), 54.5 (C<sub>α</sub>), 66.5, 66.7 (2 CH<sub>2</sub> benzyl), 128.2, 128.4, 128.6, 128.7 (10 CH Ar), 135.9, 136.7 (2 C Ar), 156.7 (CO Boc and Cbz), 172.3, 173.2 (2 CO).

**DTPA(tBu)<sub>4</sub>-Lys(Cbz)-Abu-OBn.** To a solution of Boc-Lys(Cbz)-Abu-OBn (2.78 g, 5 mmol) in CH<sub>2</sub>Cl<sub>2</sub> (20 mL), H<sub>2</sub>O (0.2 mL) and TFA (20 mL) were added, and the mixture was stirred for 1 h at room temperature. The volatiles were evaporated, and CH<sub>2</sub>Cl<sub>2</sub> and 5% NaHCO<sub>3</sub> solution were added. The layers were separated and the aqueous layer was extracted with CH<sub>2</sub>Cl<sub>2</sub>. The combined organic fractions were dried with Na<sub>2</sub>SO<sub>4</sub>, filtered, and concentrated. The obtained oil was dissolved in CH<sub>2</sub>Cl<sub>2</sub> (25 mL).

DTPA(tBu)<sub>4</sub> (3.09 g, 5 mmol) and PyBOP (2.60 g, 5 mmol) were dissolved in CH<sub>2</sub>Cl<sub>2</sub> (25 mL) and DiPEA (2.18 mL, 12.5 mmol) was added. This solution was added to the solution of H-Lys(Cbz)-Abu-OBn in CH<sub>2</sub>Cl<sub>2</sub>. The reaction mixture was stirred over the weekend at room temperature and then washed with 5% NaHCO<sub>3</sub> solution and brine, dried with Na<sub>2</sub>SO<sub>4</sub>, filtered, and concentrated. The product was purified with column chromatography (first EtOAc/hexane 1:4 with 0.5% TEA, then EtOAc/hexane 1:2 with 0.5% TEA, then EtOAc with 0.5% TEA, and then EtOAc/MeOH 1:9 with 0.5% TEA), yielding 4.6 g (4.36 mmol, 87%) of a yellow oil. MS: [M + H]<sup>+</sup> calculated 1055.3, found 1055.9. <sup>1</sup>H NMR (CDCl<sub>3</sub>, 300 MHz) δ = 1.43–1.56 (m, 40H, 2 CH<sub>2</sub>, 12 CH<sub>3</sub>), 1.77–1.91 (m, 4H, 2 CH<sub>2</sub>), 2.37 (t, 2H, CH<sub>2</sub>), 2.58–2.64 (m, 4H, 2 CH<sub>2</sub> DTPA), 2.74–2.77 (m, 4H, 2 CH<sub>2</sub> DTPA), 3.14–3.31 (m, 6H, CH<sub>2</sub> DTPA, 2 CH<sub>2</sub>), 3.36 (s, 8H, 4 CH<sub>2</sub> DTPA), 4.25–4.35 (m, 1H, CH), 5.08, 5.10 (2 s, 4H, 2 CH<sub>2</sub> benzyl), 5.20, 6.86, 8.32 (3 m, 3H, 3 NH), 7.29–7.35 (m, 10H, Ar).

**DTPA(tBu)<sub>4</sub>-Lys-Abu.** To a solution of DTPA(tBu)<sub>4</sub>-Lys(Cbz)-Abu-OBn (3.5 g, 3.32 mmol) in MeOH (50 mL)

ammonium formate (4.19 g, 66.4 mmol) and 10% Pd–C (66 mg) were added and the mixture was stirred overnight at room temperature. The suspension was filtered over Celite and concentrated. The residue was dissolved in EtOAc and washed with 5% NaHCO<sub>3</sub> solution, dried with Na<sub>2</sub>SO<sub>4</sub>, filtered, and concentrated. The product was purified with column chromatography (gradient of CH<sub>2</sub>Cl<sub>2</sub>/MeOH 4:1 with 0.5% 30–33% NH<sub>3</sub> in H<sub>2</sub>O to MeOH with 0.5% 30–33% NH<sub>3</sub> in H<sub>2</sub>O) yielding 2.17 g (2.61 mmol, 79%) of an off-white foam. MS: [M + H]<sup>+</sup> calculated 831.1, found 831.2.

**Cy5.** Cy5 was synthesized as described previously.<sup>37</sup>

**DTPA(tBu)<sub>4</sub>-Lys(Cy5)-Abu.** To a solution of Cy5 (77 mg, 100 μmol), PyBOP (52 mg, 100 μmole), and HOBt (15 mg, 100 μmol) in DMF (2 mL), DiPEA (87 μL, 500 μmol) was added and the solution was stirred for 1 h at room temperature. DTPA(tBu)<sub>4</sub>-Lys-Abu was dissolved in DMSO/DMF 1:1 (2 mL) and DiPEA (35 μL, 500 μmol) was added. This solution was added to the activated Cy5 and the resulting mixture was stirred overnight at room temperature. The crude mixture was directly purified by column chromatography (gradient of CH<sub>2</sub>Cl<sub>2</sub>/MeOH 2:1 with 1% 30–33% NH<sub>3</sub> in H<sub>2</sub>O to CH<sub>2</sub>Cl<sub>2</sub>/MeOH 1:1 with 1% 30–33% NH<sub>3</sub> in H<sub>2</sub>O). The final purification was done using preparative HPLC with a gradient of 0.1% TFA in H<sub>2</sub>O/CH<sub>3</sub>CN 9:1 to 0.1% TFA in H<sub>2</sub>O/CH<sub>3</sub>CN 1:9 in 100 min (4 runs). The product was obtained as a blue fluffy solid (32.5 mg, 20.6 μmol, 21%) after pooling of the appropriate fractions and lyophilization. MS: [M]<sup>+</sup> calculated 1579.0, found 1578.4; [M+Na–H]<sup>+</sup> calculated 1601.0, found 1601.6.

**DTPA-Cy5-UBI<sub>29–41</sub>.** UBI<sub>29–41</sub> was synthesized using solid phase peptide synthesis (SPPS) following standard Fmoc-chemistry procedures on a 10 μmol scale. After peptide synthesis, the N-terminus was deprotected on resin. DTPA-(tBu)-Lys(Cy5)-Abu (17.4 mg, 11 μmol) was preactivated with PyBOP (6.3 mg, 12 μmol), HOBt (1.9 mg, 12 μmol), and DiPEA (4.2 μL, 25 μmol) in NMP (2 mL) for 5 min before adding it to the resin-bound peptide. The resin was stirred overnight, followed by thorough washing with NMP (3 times), then DCM (3 times), and complete deprotection and cleavage from the resin by 95% TFA, 2.5% H<sub>2</sub>O, and 2.5% TIS cleavage cocktail. The precipitate was lyophilized to yield 21 mg of the crude product, which was purified by reversed phase HPLC (100 min from 95% H<sub>2</sub>O containing 0.1% TFA to 95% ACN containing 0.1% TFA). Fractions containing the product were pooled and lyophilized yielding 3 mg of the product as a fluffy blue solid. Using MS, [M]<sup>+</sup> for C<sub>127</sub>H<sub>205</sub>N<sub>40</sub>O<sub>38</sub>S<sub>4</sub><sup>+</sup> was found to be 3026.9, calculated 3026.4. Stock solutions (1.75 mg/mL) of the DTPA-Cy5-UBI<sub>29–41</sub> in 0.25 M ammonium acetate (pH 4) were stored at –20 °C.

**<sup>111</sup>In-DTPA-Cy5-UBI<sub>29–41</sub>.** A volume of 10–40 μL of the peptide solution (1.75 mg/mL in 0.25 M ammonium acetate pH 5.5) was added to an acidic solution of <sup>111</sup>InCl<sub>3</sub> (25–150 μL, 370 MBq/mL, Mallinckrodt Medical, Petten, The Netherlands) and the mixture was gently shaken in the dark for 3 h at 37 °C. Thereafter, the pH was adjusted to 7.5 using PBS. This preparation, further referred to as <sup>111</sup>In-DTPA-Cy5-UBI<sub>29–41</sub>, had a radiochemical purity of 96.3 ± 2.7% (n = 5) after analysis by instant thin layer chromatography (ITLC) on 0.5 cm × 5 cm ITLC-SG paper strips (Agilent Technologies, Amstelveen, The Netherlands) with 250 mM ammonium acetate pH 5.5 (Sigma-Aldrich, St. Louis, MO) as mobile phase. As no further purification was necessary, the preparations were ready for use. Labeling of UBI<sub>29–41</sub> with <sup>99m</sup>Tc was performed as described

before.<sup>27</sup> Additionally, we assessed the stability of <sup>111</sup>In-DTPA-Cy5-UBI<sub>29–41</sub> for 24 h after labeling using ITLC and we challenged <sup>111</sup>In-DTPA-Cy5-UBI<sub>29–41</sub> in 50% (v/v) fetal bovine serum (Gibco Fetal Bovine Serum, Life Technologies Europe BV, Bleiswijk, The Netherlands) for 24 h at 37 °C and determined release of the radiolabel with ITLC.

**Microorganisms.** Various virulent bacterial strains, either Gram-positive or Gram-negative obtained from the American Type Culture Collection (ATCC, Rockville, MD), namely, *S. aureus* ATCC 29213, *S. epidermidis* ATCC 12228, *K. pneumoniae* ATCC 43861, *E. coli* ATCC 25922, and *B. subtilis* JH642, were kindly donated by Dr. Wiep Klaas Smits (Department of Bacteriology, LUMC, Leiden, The Netherlands). Suspensions containing about 10<sup>9</sup> CFU stationary-phase bacteria per mL of BHI broth were stored at –80 °C.

#### In Vitro Binding Assay and Confocal Microscopy.

Binding of <sup>111</sup>In-DTPA-Cy5-UBI<sub>29–41</sub> to 5 bacterial strains was assessed at 4 °C as described earlier.<sup>27</sup> In short, ammonium acetate (0.25 M, 0.05 mL, pH 5.5) containing 1.0 or 1.7 μg <sup>111</sup>In-DTPA-Cy5-UBI<sub>29–41</sub> (respectively, 3.3 × 10<sup>–10</sup> mol and 5.6 × 10<sup>–10</sup> mol) or 1 μg <sup>99m</sup>Tc-UBI<sub>29–41</sub> (5.9 × 10<sup>–10</sup> mol) was mixed with the incubation buffer (0.8 mL, 50% of 0.1% (v/v) acetic acid in PBS supplemented with 0.01% (v/v) Tween-80, Sigma-Aldrich, St. Louis, MO) and PBS (1 mL, pH 5) containing bacteria (2 × 10<sup>8</sup> CFU). After 1 h incubation the bacteria were washed in PBS (2×) and the radioactivity in the pellet containing bacteria and the supernatant was determined in a dose calibrator. The radioactivity associated with bacteria was calculated as percentage of added radiolabeled UBI<sub>29–41</sub> to bacteria (2 × 10<sup>8</sup> CFU). For microscopic imaging of fluorescent labeling of bacteria, binding studies were performed under similar conditions with unlabeled DTPA-Cy5-UBI<sub>29–41</sub>. Bacteria were fixed for 1 h at 37 °C in formalin (4%), mounted in agarose (1%) on a microscope slide, which was covered and sealed. The Cy5 fluorescence was detected with a Leica SP5 confocal microscope (Leica Microsystems B.V., Eindhoven, The Netherlands).

**MTT Toxicity Assay.** To study cytotoxicity of the tracers we determined the effect of various amounts of DTPA-Cy5-UBI<sub>29–41</sub> and UBI<sub>29–41</sub> to human epithelial cells in a MTT (3-(4,5-dimethylthiazol-2-yl)-2,5-diphenyltetrazolium bromide, Sigma-Aldrich) toxicity assay.<sup>35</sup> For this purpose we seeded 4000 GE11-β3 epithelial cells in Dulbecco's Modified Eagle's Medium (DMEM, Sigma-Aldrich) containing 10% fetal bovine serum (Gibco), 100 IU/mL penicillin, and 100 mg/mL streptomycin (Invitrogen LifeSciences) per well of a transparent 96-well plate (Cellstar, Greiner Bio-One, Alphen a/d Rijn, The Netherlands) and allowed them to develop to density between 30% and 40% for 24 h.<sup>38</sup> To determine a dose dependency, after aspiration of the medium, cells were incubated with 10 dilutions between 0 and 118 μM of either DTPA-Cy5-UBI<sub>29–41</sub> or UBI<sub>29–41</sub> in medium (N = 4 for each concentration). These solutions were allowed to incubate for 4 or 24 h at 37 °C. Thereafter, the cells were inspected by microscopy and the medium was aspirated and to each well 100 μL of MTT (5 mg/mL medium) was added. For all incubations, the maximum density was 80% at the time of adding MTT. After incubation for 3 h at 37 °C, the supernatant was aspirated and replaced with 100 μL of DMSO (Sigma-Aldrich). After incubating for 15 min at 37 °C, the plate was gently shaken and the absorbance at 545 nm of reduced MTT was measured in a Victor<sup>3</sup> plate reader (1420 Multilabel Counter, PerkinElmer, Groningen The Netherlands). Values of



MTT coloring with various amounts of peptide are expressed as the normalized values calculated from incubations without UBI<sub>29–41</sub> peptide.

**Mouse Infection Model.** All in vivo studies were performed using 2–3-month-old Swiss mice (20–25 g, Crl:OF1 strain, Charles River Laboratories, Erkrath, Germany). All animal studies have been approved by the institutional Animal Ethics Committee (DEC permit 12160) of the Leiden University Medical Center. All mice were kept under specific pathogen-free conditions in the animal housing facility of the LUMC. Food and water were given ad libitum. Mice were anaesthetized with a single intraperitoneal injection of anesthetic (0.1 mL, 1 mg fluanisone, 0.03 mg fentanyl citrate, Hypnorm, Janssen Pharmaceuticals, Tilburg, The Netherlands). Approximately 0.1 mL (thigh muscle) or 0.05 mL (front paw muscle) of bacteria suspensions ( $4.0 \times 10^8$  CFU/mL) were injected into the right muscles. The infections were allowed to develop for 18 h.

**U-SPECT-BioFluo Imaging of Infections in Mice.** To study the biodistribution of the tracer, mice ( $n = 4$  for each tracer and  $n = 4$  for each type of bacteria) received an intramuscular injection of  $4 \times 10^7$  (thigh) or  $2 \times 10^7$  (front paw) CFU of either *S. aureus* or *K. pneumoniae*, as these two strains show similarity in virulence and outgrowth. Eighteen hours after inoculation, the mice were injected intravenously with  $^{111}\text{In}$ -DTPA-CyS-UBI<sub>29–41</sub> or  $^{99\text{m}}\text{Tc}$ -UBI<sub>29–41</sub> (10  $\mu\text{g}$ , 10–20 MBq) in a tail vein and imaged at various intervals after the injection. The animals were placed and fixed onto a dedicated positioned bed of a three-headed U-SPECT-BioFluo<sup>25</sup> (MILabs, Utrecht, The Netherlands) under continuous 1–2% isoflurane anesthesia. Radioactivity counts from total body scans or selected regions of interest (ROI) were acquired for 30 min using a 0.6 mm mouse multipinhole collimator in list mode data. For reconstruction from list mode data, the photopeak energy window was centered at 171 keV with a window width of 20%. Side windows of 5% were applied to correct for scatter and down scatter corrections. The image was reconstructed using 24 pixel based ordered subset expectation maximization iterations (POSEM) with 4 subsets, 0.2 mm isotropic voxel size and with decay and triple energy scatter correction integrated into the reconstruction with a post filter setting of 0.25 mm.<sup>39</sup> Volume-rendered images were generated from 2 to 4 mm slices and analyzed using *Matlab R2014a* software (v 8.3.0.532, MathWorks Natick, MA). Images were generated from maximum intensity protocols (MIP) adjusting the color scale threshold to optimal depiction of the infected tissues.<sup>25</sup> Thereafter, fluorescence imaging of infected muscles was performed under the optical hood of the U-SPECT-BioFluo (MILabs) imaging system under continuous 1–2% isoflurane anesthesia. The exposure time for the fluorescence measurement was 300 ms with the appropriate filters set for Cy5 dye as described.<sup>25</sup>

**CT Imaging of Mice.** As a reference for the localization of the infection, after imaging the mice in the U-SPECT-BioFluo camera the animal bed was transferred to the animal positioning bed of the microcomputed tomography (microCT) system. CT-scans (SkyScan 1076 microCT scanner, Bruker/Skyscan, Kontich, Belgium) using a source voltage of 40 kV and a source current of 250 mA, with a step size of 1.3 deg over a trajectory of 180 deg plus fan angle) were used to provide anatomical context for the SPECT findings. Images were taken with a frame average of 2 to reduce noise and an image pixel size of 35  $\mu\text{m}$ . Reconstructions were made using *NRecon*

software (SkyScan v 1.6.9.8), with a beam hardening correction set to 26% and a ring artifact correction set to 5. Images were analyzed using *CTvox* software (Bruker microCT v 2.7.0 r990, 64 bit).

**Fluorescent Imaging of Infections in Mice.** Fluorescence imaging of infected muscles was performed using the IVIS Spectrum (Caliper Life Science, Hopkinton, MA) imaging system under continuous 1–2% isoflurane anesthesia. Images of areas containing the infected muscles after removing the fur and skin were acquired following excitation at 640 nm, and light was collected between >700 nm (acquisition time 1 or 2 s). To deal with the high amounts of tracer in the kidneys and urinary bladder during imaging, signals from these organs were masked with black paper. Data analysis of the IVIS Spectrum data was performed using the *Living Image* software from xenogeny v 3.2 (Caliper LS). Multiple regions of interest (ROI) were drawn in the infected muscles (target, T) and in adjacent noninfected muscles (nontarget, NT); these values were divided to calculate T/NT ratios. Thereafter, the animals were euthanized by intraperitoneal injection of Euthasol (0.25 mL, 200 mg/mL pentobarbital sodium, Euthasol; AST Pharma, Oudewater, The Netherlands) and various organs were removed and imaged with the IVIS Spectrum as described above.

**Biodistribution Studies.** To study the biodistribution of the hybrid tracer, animals were injected intravenously (tail vein) with  $^{111}\text{In}$ -DTPA-CyS-UBI<sub>29–41</sub> or  $^{99\text{m}}\text{Tc}$ -UBI<sub>29–41</sub> (10  $\mu\text{g}$ , 10–20 MBq). The total injected dose (ID) in each mouse was determined by counting the full and empty syringes in a dose-calibrator (VDC101, Veenstra Instruments, Joure, The Netherlands). At various intervals postinjection of the tracer, the mice were euthanized with Euthasol (0.25 mL). To determine the biodistribution of the tracer, organs were collected from mice at 2 h post injection and counted for radioactivity (Wizard2 2470 automatic gamma scintillation counter, PerkinElmer). Besides the mice for the biodistribution studies, extra animals were infected in the paw and thigh muscles to acquire time-dependent accumulation ex vivo data of the tracer 1, 2, and 24 h after injection. For both tracers, at various intervals after injection we collected blood samples of 5  $\mu\text{L}$  from a tail vein to determine the blood half-life. After collecting and counting all tissues, excreted urine and feces together with the remaining activity in the entire carcass was counted to determine the total radioactivity still present in the animal and, after correction for decay, the excretion was expressed as the percentage of the total injected dose ( $n = 4$  mice for each tracer and bacterial strain). After decay correction, radioactivity counts in tissues were expressed as the percentage of the total injected dose of radioactivity per gram (%ID/g). Next, organs were imaged in the IVIS Spectrum imager to visualize the fluorescence.

**Histology, Light, and Fluorescence Confocal Microscopy.** After ex vivo fluorescent imaging, 1 mm slices were taken from the middle region of the resected muscles using an Alto Acrylic 1 mm tissue slicing matrice (CellPoint Scientific, Gaithersburg, MD). These slides were applied on a microscopic slide for fluorescence confocal laser scanning microscopy. Half of the slices was frozen in liquid nitrogen and the other half was fixed overnight in 4% formalin and embedded in paraffin blocks. Tissues were sliced at 10  $\mu\text{m}$  adjacent from the 1 mm intersection for cryosections and stored at  $-20^\circ\text{C}$  or cut at 6  $\mu\text{m}$  thickness for paraffin sections from the other intersection of the muscle. Cryosections were defrosted and imaged using a confocal fluorescent microscope (Leica TCS SPII AOBs) at various magnifications. Images were acquired following

excitation at 633 nm and emission was collected from 650 to 750 nm. Images were further analyzed using Leica Confocal Software. Histologic sections were stained with standard hematoxylin–eosin (HE) stain or Gram staining for location of bacteria.

After counting for radioactivity and fluorescence, part of the excised infected muscles was homogenized and serial dilutions were cultured on BHI agar plates to determine the number of bacteria in these tissues.

**Statistical Analysis.** Analytical data were expressed as mean and standard error of the mean ( $\pm$ SEM) as calculated using *Microsoft Excel* software. In this study, significance of two mean values was calculated by Student-*t* test. The level of significance was set at  $p < 0.05$ .

## ■ ASSOCIATED CONTENT

### Supporting Information

Additional figures and spectra. This material is available free of charge via the Internet at <http://pubs.acs.org>.

## ■ AUTHOR INFORMATION

### Corresponding Author

\*E-mail: F.W.B.van\_leeuwen@lumc.nl.

### Author Contributions

#Mick M. Welling and Anton Bunschoten contributed equally to this work.

### Notes

The authors declare no competing financial interest.

## ■ ACKNOWLEDGMENTS

We acknowledge Ineke Heezen, Rob Krueger, and Matthias van Oosterom for technical assistance and Dr. Wiep Klaas Smits for donating bacterial strains and providing culturing media. This research was financially supported by the European Research Council under the European Union's Seventh Framework Programme (FP7/2007-2013)/ERC grant agreement n° 2012-306890, a Koningin Wilhelmina Fonds (KWF) translational research award (Grant No. PGF 2009-4344), and by The Netherlands Organisation for Scientific Research (NWO; STW BGT 11272).

## ■ REFERENCES

- (1) Esposito, S., and Leone, S. (2008) Prosthetic joint infections: microbiology, diagnosis, management and prevention. *Int. J. Antimicrob. Agents* 32, 287–293.
- (2) Wilson, J., and Elgohari, N. (2009) *Fifth Report of the Mandatory Surveillance of Surgical Site Infection in Orthopaedic Surgery, April 2004 to March 2009*, London.
- (3) Gaca, J. G., Sheng, S., Daneshmand, M. A., O'Brien, S., Rankin, J. S., Brennan, J. M., Hughes, G. C., Glower, D. D., Gammie, J. S., and Smith, P. K. (2011) Outcomes for endocarditis surgery in North America: A simplified risk scoring system. *J. Thor. Cardiovasc. Surg.* 141, 98–106.
- (4) Walter, C. J., Dumville, J. C., Sharp, C. A., and Page, T. (2012) Systematic review and meta-analysis of wound dressings in the prevention of surgical-site infections in surgical wounds healing by primary intention. *Br. J. Surg.* 99, 1185–1194.
- (5) Gemmel, F., Dumarey, N., and Welling, M. (2009) Future diagnostic agents. *Semin. Nucl. Med.* 39, 11–26.
- (6) Palestro, C. J. (2014) Nuclear medicine and the failed joint replacement: Past, present, and future. *World J. Radiol.* 6, 446–458.
- (7) Bunschoten, A., Welling, M. M., Termaat, M. F., Sathekge, M., and van Leeuwen, F. W. B. (2013) Development and prospects of

dedicated tracers for the molecular imaging of bacterial infections. *Bioconjugate Chem.* 24, 1971–1989.

- (8) Sasser, T. A., Van Avermaete, A. E., White, A., Chapman, S., Johnson, J. R., Van, A. T., Gammon, S. T., and Leevy, W. M. (2013) Bacterial infection probes and imaging strategies in clinical nuclear medicine and preclinical molecular imaging. *Curr. Top. Med. Chem.* 13, 479–487.

- (9) Welling, M. M., Paulusma-Annema, A., Balter, H. S., Pauwels, E. K. J., and Nibbering, P. H. (2000) Technetium-99m labelled antimicrobial peptides discriminate between bacterial infections and sterile inflammations. *Eur. J. Nucl. Med.* 27, 292–301.

- (10) Arteaga de, M. C., Gemmel, F., and Balter, J. (2010) Clinical trial of specific imaging of infections. *Nucl. Med. Commun.* 31, 726–733.

- (11) Brouwer, C. P., Sarda-Mantel, L., Meulemans, A., Le, G. D., and Welling, M. M. (2008) The use of technetium-99m radiolabeled human antimicrobial peptides for infection specific imaging. *Mini. Rev. Med. Chem.* 8, 1039–1052.

- (12) Ebenhan, T., Chadwick, N., Sathekge, M. M., Govender, P., Govender, T., Kruger, H. G., Marjanovic-Painter, B., and Zeevaart, J. R. (2014) Peptide synthesis, characterization and  $^{68}\text{Ga}$ -radiolabeling of NOTA-conjugated ubiquitin fragments for prospective infection imaging with PET/CT. *Nucl. Med. Biol.* 41, 390–400.

- (13) Liu, C., and Gu, Y. (2013) Noninvasive optical imaging of *Staphylococcus aureus* infections in vivo using an antimicrobial peptide fragment based near-infrared fluorescent probes. *J. Innov. Opt. Health Sci.* 06, 1350026.

- (14) van der Poel, H. G., Buckle, T., Brouwer, O. R., Valdes Olmos, R. A., and van Leeuwen, F. W. B. (2011) Intraoperative laparoscopic fluorescence guidance to the sentinel lymph node in prostate cancer patients: clinical proof of concept of an integrated functional imaging approach using a multimodal tracer. *Eur. Urol.* 60, 826–833.

- (15) Brouwer, O. R., Buckle, T., Vermeeren, L., Klop, W. M., Balm, A. J., van der Poel, H. G., van Rhijn, B. W., Horenblas, S., Nieweg, O. E., van Leeuwen, F. W. B., et al. (2012) Comparing the hybrid fluorescent-radioactive tracer indocyanine green-99mTc-nanocolloid with 99mTc-nanocolloid for sentinel node identification: a validation study using lymphoscintigraphy and SPECT/CT. *J. Nucl. Med.* 53, 1034–1040.

- (16) Chin, P. T., Welling, M. M., Meskers, S. C., Valdes Olmos, R. A., Tanke, H., and van Leeuwen, F. W. B. (2013) Optical imaging as an expansion of nuclear medicine: Cerenkov-based luminescence vs fluorescence-based luminescence. *Eur. J. Nucl. Med. Mol. Imaging* 40, 1283–1291.

- (17) Kuil, J., Velders, A. H., and van Leeuwen, F. W. B. (2010) Multimodal tumor-targeting peptides functionalized with both a radio- and a fluorescent label. *Bioconjugate Chem.* 21, 1709–1719.

- (18) Kuil, J., Buckle, T., Yuan, H., van den Berg, N. S., Oishi, S., Fujii, N., Josephson, L., and van Leeuwen, F. W. B. (2011) Synthesis and evaluation of a bimodal CXCR4 antagonistic peptide. *Bioconjugate Chem.* 22, 859–864.

- (19) Bunschoten, A., Buckle, T., Visser, N. L., Kuil, J., Yuan, H., Josephson, L., Vahrmeijer, A. L., and van Leeuwen, F. W. B. (2012) Multimodal interventional molecular imaging of tumor margins and distant metastases by targeting  $\alpha_5\beta_3$  integrin. *ChemBioChem* 13, 1039–1045.

- (20) van den Berg, N. S., Buckle, T., Kleinjan, G. I., Klop, W. M., Horenblas, S., van der Poel, H. G., Valdes-Olmos, R. A., and Van Leeuwen, F. W. B. (2014) Hybrid tracers for sentinel node biopsy. *Q. J. Nucl. Med. Mol. Imaging* 58, 193–206.

- (21) Lewis, S. S., Cox, G. M., and Stout, J. E. (2014) Clinical utility of indium 111-labeled white blood cell scintigraphy for evaluation of suspected infection. *Open. Forum Infect. Dis.* 1, ofu089.

- (22) Shao, F., Yuan, H., Josephson, L., Weissleder, R., and Hilderbrand, S. A. (2011) Facile synthesis of monofunctional pentamethine carbocyanine fluorophores. *Dyes Pigm.* 90, 119–122.

- (23) Wadas, T. J., Wong, E. H., Weisman, G. R., and Anderson, C. J. (2010) Coordinating radiometals of copper, gallium, indium, yttrium,

and zirconium for PET and SPECT imaging of disease. *Chem. Rev.* 110, 2858–2902.

(24) Burggraaf, J., Kamerling, I. M. C., Gordon, P. B., Schrier, L., de Kam, M. L., Kales, A. J., Bendiksen, R., Indrevoll, B., Bjerke, R. M., Moestue, S. A., et al. (2014) Detection of colorectal polyps using an intravenously administered fluorescent peptide targeted against c-Met, *Nat. Med.*, Accepted for publication.

(25) van Oosterom, M. N., Kreuger, R., Buckle, T., Mahn, W. A., Bunschoten, A., Josephson, L., van Leeuwen, F. W. B., and Beekman, F. J. (2014) U-SPECT-BioFluo: an integrated radionuclide, bioluminescence, and fluorescence imaging platform. *EJNMMI Res.* 4, 56.

(26) Yeaman, M. R., and Yount, N. Y. (2003) Mechanisms of antimicrobial peptide action and resistance. *Pharmacol. Rev.* 55, 27–55.

(27) Welling, M. M., Mongera, S., Lupetti, A., Balter, H. S., Bonetto, V., Mazzi, U., Pauwels, E. K. J., and Nibbering, P. H. (2002) Radiochemical and biological characteristics of  $^{99m}\text{Tc}$ -UBI 29–41 for imaging of bacterial infections. *Nucl. Med. Biol.* 29, 413–422.

(28) Ellerby, H. M., Arap, W., Ellerby, L. M., Kain, R., Andrusiak, R., Rio, G. D., Krajewski, S., Lombardo, C. R., Rao, R., Ruoslahti, E., et al. (1999) Anti-cancer activity of targeted pro-apoptotic peptides. *Nat. Med.* 5, 1032–1038.

(29) Sarda-Mantel, L., Saleh-Mghir, A., Welling, M. M., Meulemans, A., Vrigneaud, J. M., Raguin, O., Hervatin, F., Martet, G., Chau, F., Lebtahi, R., et al. (2007) Evaluation of  $^{99m}\text{Tc}$ -UBI 29–41 scintigraphy for specific detection of experimental *Staphylococcus aureus* prosthetic joint infections. *Eur. J. Nucl. Med. Mol. Imaging* 34, 1302–1309.

(30) Welling, M. M., Visentin, R., Feitsma, H. I. J., Lupetti, A., Pauwels, E. K. J., and Nibbering, P. H. (2004) Infection detection in mice using  $^{99m}\text{Tc}$ -labeled HYNIC and  $\text{N}_2\text{S}_2$  chelate conjugated to the antimicrobial peptide UBI 29–41. *Nucl. Med. Biol.* 31, 503–509.

(31) Welling, M. M., Ferro-Flores, G., Pirmettis, I., and Brouwer, C. P. J. M. (2009) Current status of imaging infections with radiolabeled anti-infective agents. *Anti-Infect. Agents Med. Chem.* 8, 272–287.

(32) Chin, P. T., Beekman, C. A., Buckle, T., Josephson, L., and van Leeuwen, F. W. B. (2012) Multispectral visualization of surgical safety-margins using fluorescent marker seeds. *Am. J. Nucl. Med. Mol. Imaging* 2, 151–162.

(33) Brouwer, C. P. J. M., Bogaards, S. J. P., Wulferink, M., Velders, M. P., and Welling, M. M. (2006) Synthetic peptides derived from human antimicrobial peptide ubiquicidin accumulate at sites of infections and eradicate (multi-drug resistant) *Staphylococcus aureus* in mice. *Peptides* 27, 2585–2591.

(34) Ostovar, A., Assadi, M., Vahdat, K., Nabipour, I., Javadi, H., Eftekhari, M., and Assadi, M. (2013) A pooled analysis of diagnostic value of  $^{99m}\text{Tc}$ -ubiquicidin (UBI) scintigraphy in detection of an infectious process. *Clin. Nucl. Med.* 38.

(35) Berridge, M. V., and Tan, A. S. (1993) Characterization of the cellular reduction of 3-(4,5-dimethylthiazol-2-yl)-2,5-diphenyltetrazolium bromide (MTT): subcellular localization, substrate dependence, and involvement of mitochondrial electron transport in MTT reduction. *Arch. Biochem. Biophys.* 303, 474–482.

(36) Nibbering, P. H., Welling, M. M., Paulusma-Annema, A., Brouwer, C. P., Lupetti, A., and Pauwels, E. K. (2004)  $^{99m}\text{Tc}$ -labeled UBI 29–41 peptide for monitoring the efficacy of antibacterial agents in mice infected with *Staphylococcus aureus*. *J. Nucl. Med.* 45, 321–326.

(37) Mujumdar, R. B., Ernst, L. A., Mujumdar, S. R., Lewis, C. J., and Waggoner, A. S. (1993) Cyanine dye labeling reagents: sulfoindocyanine succinimidyl esters. *Bioconjugate Chem.* 4, 105–111.

(38) Huveneers, S., van den Bout, I., Sonneveld, P., Sancho, A., Sonnenberg, A., and Danen, E. H. J. (2007) Integrin  $\alpha\text{v}\beta 3$  controls activity and oncogenic potential of primed c-Src. *Cancer Res.* 67, 2693–2700.

(39) Branderhorst, W., Vastenhouw, B., and Beekman, F. J. (2010) Pixel-based subsets for rapid multi-pinhole SPECT reconstruction. *Phys. Med. Biol.* 55, 2023–2034.